

1 **The use of ASH-15 flowstone as a matrix-matched reference material for laser-ablation**  
2 **U-Pb geochronology of calcite**

3 Perach Nuriel<sup>1</sup>, Jörn-Frederik Wotzlaw<sup>2</sup>, Maria Ovtcharova<sup>3</sup>, Anton Vaks<sup>1</sup>, Ciprian Stremtan<sup>4</sup>,  
4 Martin Šala<sup>5</sup>, Nick M. W. Roberts<sup>6</sup>, and Andrew R. C. Kylander-Clark<sup>7</sup>

5

6 <sup>1</sup> Geological Survey of Israel, 32 Yeshayahu Leibowitz St. Jerusalem, 9692100, Israel

7 <sup>2</sup> Institute of Geochemistry and Petrology, ETH Zurich, Clausiusstrasse 25 I CH-8092 Zurich,  
8 Switzerland

9 <sup>3</sup> Department of Earth Sciences, University of Geneva, Geneva, Switzerland

10 <sup>4</sup> Teledyne Photon Machines, 384 Gallatin Park Drive, Bozeman, MT 59715, USA

11 <sup>5</sup> Department of Analytical Chemistry, National Institute of Chemistry, Hajdrihova 19, SI-1000  
12 Ljubljana, Slovenia.

13 <sup>6</sup> Geochronology and Tracers Facility, British Geological Survey, Environmental Science  
14 Centre, Nottingham, NG12 5GG, UK

15 <sup>7</sup> Department of Earth Science, University of California, Santa Barbara, CA 93106, USA.

16

17 **Abstract**

18 Latest advances in laser ablation inductively coupled plasma mass spectrometer (LA-ICPMS)  
19 allow for accurate *in-situ* U-Pb dating of carbonate material, with final age uncertainties usually  
20 >3%  $2\sigma$ . Cross-laboratory reference materials (RMs) used for sample-bracketing are currently  
21 limited to WC1 calcite with an age of  $254.4 \pm 6.5$  ( $2\sigma$ ). The minimum uncertainty on any age  
22 determination with the LA-ICPMS method is therefore  $\geq 2.5\%$ , and validation by secondary  
23 RMs is usually performed on in-house standards. This contribution present a new reference  
24 material, ASH-15, a flowstone that is dated here by isotope dilution (ID) TIMS analysis using  
25 37 sub-samples, 1-7 mg each. Age results presented here are slightly younger compared to

26 previous ID-IRMS U-Pb dates of ASH-15, but within uncertainties and in agreement with *in-*  
27 *situ* analyses using WC1 as the primary RM. We provide new correction parameters to be used  
28 as primary or secondary standardization. The suggested  $^{238}\text{U}/^{206}\text{Pb}$  apparent age, not corrected  
29 for disequilibrium and without common-lead anchoring, is  $2.965 \pm 0.011$  Ma ( $2\sigma$ ). The new  
30 results could improve the propagated uncertainties on the final age with a minimal value of  
31 0.4%, which is approaching the uncertainty of typical ID analysis on higher-U materials such  
32 as zircon. We show that although LA-ICPMS spot analyses of ASH-15 exhibit significant  
33 scatter in their isotopic ratios, the down-hole fractionation of ASH-15 is similar to that of other  
34 reference materials. This high-U ( $\sim 1$  ppm) and low Pb ( $< 0.01$  ppm) calcite is most appropriate  
35 as a reference material for other speleothem-type carbonates but requires sensitive sector-field  
36 ICP-MS instruments. Reference materials with high Pb and low U or both low U and Pb  
37 compositions are still needed to fully cover the compositional range of carbonate material but  
38 may introduce analytical challenges.

## 39 **Introduction**

40 Recent advances in laser ablation techniques applied to multi-phase carbonates allow for  
41 accurate dating of a variety of sample types, including calcite cements (Li et al., 2014; Godeau  
42 et al., 2018; Anjiang et al., 2019; Holdsworth et al., 2019), hydrothermal veins (Coogan et al.,  
43 2016; MacDonald et al., 2019; Piccione et al., 2019), fault-related veins, breccia cement, and  
44 slickenfibers (Ring and Gerdes, 2016; Roberts and Walker, 2016; Goodfellow et al., 2017;  
45 Nuriel et al., 2017; Hansman et al., 2018; Parrish et al., 2018; Nuriel et al., 2019), and  
46 speleothems (Woodhead and Petrus, 2019). With increasing attention to climatic, seismic, and  
47 environmental events in the geological record, there is a growing need for dating techniques  
48 that can be accurate and easily implemented for samples at the sub-millimeter scale. This newly  
49 emerging technique has the potential to contribute to our understanding of the duration, rate,  
50 and extent of these important events in the geological record.

51 The *in-situ* approach has a great research potential for studying texturally complex samples  
52 because it can resolve problems of age mixing of different phases or averaging of continuous  
53 growth at the sub-millimeter scale, and thus increase the overall accuracy of the dated material.  
54 While the precision of traditional isotope-dilution (ID) U-Pb analyses is still favorable (<1%  
55  $2\sigma$ ) (Woodhead and Petrus, 2019), the increasing analytical development of the LA-ICPMS  
56 method indicates the potential for improving the currently reported uncertainties (usually >3%  
57  $2\sigma$ ). Finding the right matrix-matched reference material (RM) is a major hurdle for LA  
58 analyses of carbonates because of the variety of mineralogy (calcite, dolomite, and aragonite),  
59 textures, composition (e.g. high-magnesium calcite, high common-lead), and ages (e.g. low  
60 radiogenic lead in young samples). Textural differences such as microcrystalline, fine- and  
61 coarse-grained material, between the unknown and RMs can contribute to high uncertainties  
62 due to differences in ablation efficiency, down-hole fractionation, and differences in crater  
63 morphology (e.g. Guillong et al., 2020 and Elisha et al, 2020, this issue). Observed deviations  
64 are potentially up to 20% of the final intercept age depending on the degree of crater geometry  
65 mismatch and are related either to downhole fractionation and/or matrix effects (Guillong et  
66 al., 2020).

67 Currently, the most commonly used procedure for mass-bias correction in the LA method, is  
68 by standard-sample bracketing. For this, the  $^{238}\text{U}/^{206}\text{Pb}$  LA-age of the RMs is corrected to the  
69 true RM's  $^{238}\text{U}/^{206}\text{Pb}$  apparent age (not corrected for disequilibrium) as measured  
70 independently by an ID-IRMS method (ID-TIMS or ID-MC-ICPMS). The RMs are measured  
71 throughout each session along with the unknown samples, and a normalization factor is applied  
72 to correct both the RMs and the unknowns. Uncertainty propagation onto the age of the  
73 unknowns includes the uncertainties of the 'true' RM age. As a result, the accuracy of the LA  
74 analyses can only be as good as the uncertainties on the age of the RMs which is by itself  
75 subjected to analytical challenges due to natural heterogeneities, impurities, and textural

76 complexities at the sub-millimetre scale. It is therefore essential that the ‘true age’ of the  
77 reference material will reflect these complexities while maintaining minimal uncertainties.

78 Currently, several in-house standards are being used as reference materials, including Duff  
79 Brown Tank (64 Ma; Hill et al., 2016), and JT ( $13.797 \pm 0.031$  Ma; Guillong et al., 2020). The  
80 only well-characterized reference material that is distributed across laboratories is the WC1  
81 calcite with an age of  $254.4 \pm 6.5$  2s (2.5%) (Roberts et al., 2017). The use of WC1 alone for  
82 mass-bias correction has several disadvantages. First, it is highly recommended with all in situ  
83 U-Th-Pb geochronology to use secondary RMs to validate any correction parameters that are  
84 being used, and to appropriately propagate uncertainties. Second, the relatively high  
85 uncertainty (2.5%) on the age of WC1 sets a minimal uncertainty on any LA U-Pb age  
86 determination. Finally, the quantity of the WC1 sample that is currently available for future  
87 work is limited and is likely to not fully meet the growing demands of the LA scientific  
88 community; although we note here that there is a potential for further sample collection from  
89 the original site.

90 This contribution introduces a new carbonate reference material that can be widely used for *in-*  
91 *situ* dating of calcite as primary or as cross-reference material with other available standards.  
92 We characterise the reference material at various resolutions using a combination of (1) laser  
93 ablation imaging (20  $\mu\text{m}$  square beam); (2) LA spot analysis,  $\sim 80\text{-}110$   $\mu\text{m}$  in diameter,  
94 conducted on both multi-collector (MC) and single collector inductively coupled plasma mass  
95 spectrometer (ICPMS); and (3) ID-TIMS analyses of 37 sub-samples ( $\sim 1\text{-}7$  mg aliquots). We  
96 discuss several key issues related to the use of ASH-15 sample as a RM, including down-hole  
97 fractionation, heterogeneities, and previous bulk analyses, to provide the best correction  
98 parameters and suggested protocols for users of the LA scientific community.

99

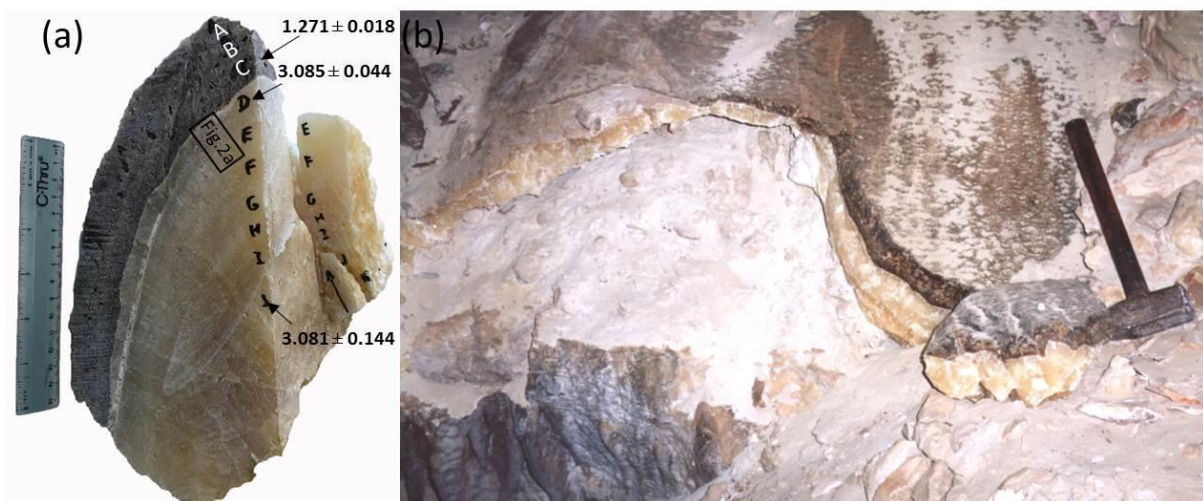
100 **1. The ASH-15 flowstone**

101 The ASH-15 flowstone was found in Ashalim Cave, a karstic cave in the central Negev Desert  
102 (30°56'36.2" N, 34°44'22.5" E), southern Israel, which is part of the northern margin of the  
103 Saharan–Arabian desert belt. The cave entrance is located at an elevation of 414 m above sea  
104 level and 67 km SE from the Mediterranean Sea coast. The cave is a three-dimensional  
105 hypogene maze with a total length of 540 m, situated in Turonian limestone rock strata, at  
106 depths of 0-31 m below the surface. The cave is richly decorated with vadose speleothems,  
107 such as stalagmites, stalactites and flowstone, which are not active today because of the aridity  
108 of the climate in the area (Vaks et al, 2010, 2018), but periods of their deposition correspond  
109 to past episodes of wet climate in present-day desert. The thickness of the speleothems varies  
110 from several cm to a few tens of cm. The soil above the cave is silicate loess, originated mainly  
111 from aeolian dust (Crouvi et al., 2010) and the present day vegetation is composed of sparse  
112 xeric shrubs with <10% vegetation cover.

113 The vadose speleothems of Ashalim Cave are composed of low-Mg calcite, and are divided  
114 into a relatively thick Pliocene Basal layer, and thinner Pleistocene layers above it. The Basal  
115 layer varies from 5 to 25 cm in thickness and comprises c. 90% of the speleothem volume in  
116 the cave. It is composed of massive yellow calcite crystals (Fig. 1a-b), often showing  
117 continuous growth in stalagmites and flowstone, suggesting deposition from continuously  
118 dripping water. In all speleothems the Basal layer is terminated at its top by a <1 mm layer of  
119 microcrystalline calcite, evaporite minerals and reddish clays (Fig. 1a), that is interpreted as a  
120 hiatus (growth break) separating the Basal Pliocene layer and Quaternary layers above it (Vaks  
121 et al., 2013). The thickness of Pleistocene top layers varies from several mm to 17 cm, but  
122 usually does not exceed a few cm, comprising about 10% of the speleothem volume in the cave.  
123 It is composed of alternating layers of brown calcite, with the youngest top layer (where found)  
124 composed of yellow calcite. Several variably colored layers <1 mm thick of microcrystalline

125 calcite, evaporite minerals and reddish clays are found within the columnar crystalline structure,  
126 suggesting hiatuses in speleothem deposition (Vaks et al., 2013).

127 The youngest periods of speleothem deposition in several Ashalim Cave speleothems were  
128 dated by the  $^{238}\text{U}$ - $^{230}\text{Th}$  method and occurred from 221 ka to 190 ka and from 134 to 114 ka  
129 (Vaks et al, 2010). Earlier periods of deposition were dated by the U-Pb method on ASH-15  
130 flowstone at  $1.272 \pm 0.018$  Ma (ASH-15-C), and the Basal layer of ASH-15 flowstone (layers  
131 D-K) at c.  $\sim 3.1$  Ma (Fig 1a). These layers have been dated in three different labs following  
132 several protocols for ID analysis (Vaks et al., 2013; Mason et al., 2013). The U concentrations  
133 in speleothem calcite range between 1.9 and  $19.7 \mu\text{g/g}$  and the amounts of non-radiogenic Th  
134 are negligible (Vaks et al., 2010).

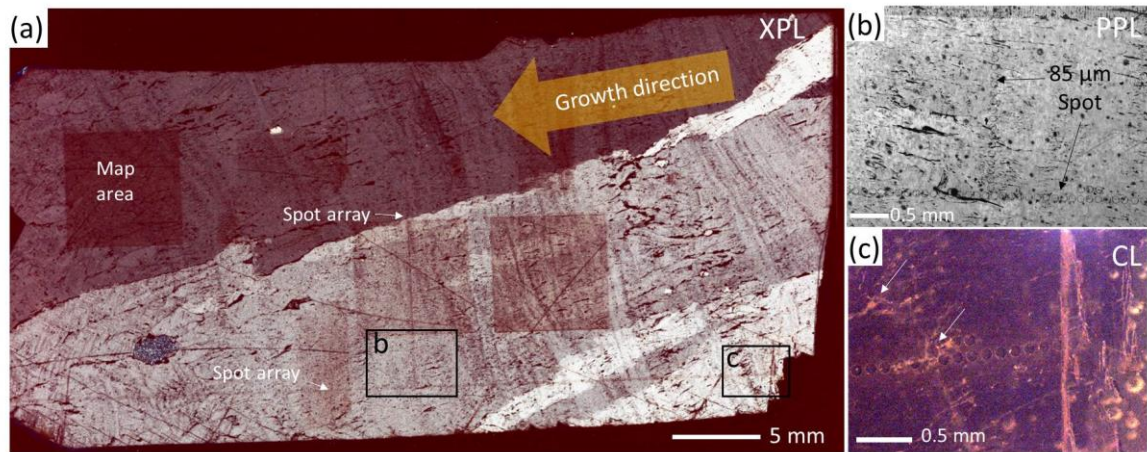


135  
136 **Figure 1.** Sample ASH-15 from Ashalim Cave. (a)  $\sim 5$  kg block of sample ASH-15 flowstone  
137 consisting of the massive Pliocene yellow Basal layer ( $>2$  cm calcite crystals; section D–K)  
138 and the brown Quaternary layer (top section, A–C), the thin layer between the two stratigraphic  
139 members represents a growth break (hiatus). The main U-Pb ages of Vaks et al., 2013 are  
140 indicated; (b) In-situ flowstone within Ashalim Cave from which ASH-15 was sampled,  
141 showing the large reservoir of this flowstone.

142

## 143 2. Sample ASH-15 textural characterization

144 The ASH-15 thin-section includes section D and E (see location in Fig.1a). Overall the thin-  
145 section examination indicates that the original texture is preserved with consistent growth  
146 direction, no observed hiatus, and no indications for dissolution and recrystallization. A spot  
147 analysis array, 85  $\mu\text{m}$  in diameter, targeted along growth zone and along growth direction is  
148 visible in Fig. 2a-c. The ASH-15 sample shows no luminescence under cathodoluminescence  
149 light (Fig. 2c), suggesting formation under oxidising conditions. The slight bright luminescence  
150 observed within grain boundaries, discontinuities, and veins (arrows in Fig. 2b-c) may suggest  
151 the presence of fluid inclusions, textural differences, or some local replacement within these  
152 areas. These areas should be avoided if possible during spot analysis. The relatively  
153 homogenous low luminescence may suggest for a single-phase continuous calcite growth,  
154 whereby precipitation occurred relatively rapid from the same fluid source (e.g. with consistent  
155  $\text{Mn}^{2+}$   $\text{Fe}^{2+}$  composition) and/or under similar precipitation redox conditions. This 15 cm thick,  
156 ~3 Ma Pliocene layer (section D-K) is essentially of the same age. For this reason, previous  
157 dating of this sample also considered a similar initial  $^{234}\text{U}/^{238}\text{U}$  activity ratio for disequilibrium  
158 correction (Mason et al., 2013; Vaks et al., 2013). The ASH-15 reference material consists of  
159 the whole Pliocene section that terminates with a sharp transition to the darker Pleistocene  
160 layers above it (section A-C; see Fig. 1b). About 3 kg of ASH-15 sample are excavated from  
161 the Ashalim Cave (Fig. 1a), and potentially much more can be sampled in the future (we  
162 estimate more than 10 kg of sample; Fig. 1b). The ASH-15 flowstone is therefore a good  
163 candidate for a reference material because of its large volume, high U concentrations, and  
164 potentially homogenous age which will be examine next.



165

166 **Figure 2.** ASH-15D-E thin-section. (a) cross-polarized (XPL) scan , 36 mm long, showing  
 167 continuous growth (no hiatus), and consistent growth direction (indicated with yellow arrow).  
 168 Spot analyses are targeted either sub-parallel to growth zone or sub-parallel to growth direction;  
 169 (b) close-up on spot array analyses (location is shown in a) with 85 μm diameter; (c) CL image  
 170 showing no luminescence except for some bright luminescence within grains boundaries and  
 171 veins (arrows).

172 **3. Methods**

173 **3.1. Elemental mapping**

174 The sample ASH-15 was cut perpendicular to the growth zone of section D and E (see Fig.1b)  
 175 in order to examine heterogeneities across growth zone and within. Thin-sections were then  
 176 examined under plane- and cross-polarized light (XPL/PPL), and cathodoluminescence (CL)  
 177 microscopy (Fig. 2). The central part of the thin-section was also analyzed for elemental  
 178 distribution of selected elements. The elemental maps were measured via LA-ICPMS, carried  
 179 out on a 193 nm ArF excimer laser ablation system (Analyte G2 Teledyne Photon Machines  
 180 Inc., Bozeman MT) coupled to an ICP-QMS (Agilent 7900, Agilent Technologies, Santa Clara  
 181 CA). The laser was equipped with a Photon Machines HelEx II ablation chamber and an  
 182 Aerosol Rapid Introduction System (ARIS). The experiments were carried out using  
 183 acquisition parameters (both on the ICP and on the laser) modelled using the approach of van



184 Elteren et al (2019; 2018) to avoid artefacts (e.g., aliasing, smear, blur). All images (500x500  
185 pixels) were acquired using a 20  $\mu\text{m}$  square beam, fluence of 3.5  $\text{Jcm}^{-2}$ , 294 Hz repetition rate  
186 and dosage of 10 (10 overlapping pulses per spot size which amount to a scanning speed of  
187 588  $\mu\text{ms}^{-1}$ ). The masses monitored were  $^{88}\text{Sr}$ ,  $^{137}\text{Ba}$ ,  $^{206}\text{Pb}$ ,  $^{208}\text{Pb}$ ,  $^{232}\text{Th}$ , and  $^{238}\text{U}$  and the  
188 images were constructed using Photon Machines' HDIP data reduction software (van Malderen,  
189 2017).

### 190 3.2. LA-MC-ICPMS spot analyses

191 A thin section of ASH-15 was dated by U-Pb laser ablation multi-collector inductively coupled  
192 plasma mass spectrometry (LA-MC-ICPMS) following the method described in Nuriel et al.  
193 (2017). A Nu Plasma 3D was employed in conjunction with a Photon Machines Excite 193nm  
194 Excimer laser equipped with a HelEx two volume cell. The laser was fired for 15 s during  
195 analysis, using a repetition rate of 10 Hz, a spot size of 85  $\mu\text{m}$ , and a fluence of approx. 1  $\text{J}/\text{cm}^2$ .  
196 The Nu Plasma 3D allows for the simultaneous acquisition of  $^{238}\text{U}$ ,  $^{235}\text{U}$ ,  $^{232}\text{Th}$ ,  $^{208}\text{Pb}$ ,  $^{207}\text{Pb}$ ,  
197  $^{206}\text{Pb}$ ,  $^{204}\text{Pb}(\text{+Hg})$ , and  $^{202}\text{Hg}$ , where  $^{238}\text{U}$ - $^{232}\text{Th}$  are measured on Faraday detectors and the low-  
198 side masses are measured on Daly detectors. Instrumental mass-bias was corrected using a  
199 two-step approach: both the  $^{207}\text{Pb}/^{206}\text{Pb}$  and  $^{206}\text{Pb}/^{238}\text{U}$  ratios were first corrected to NIST-614  
200 glass reference material in *Iolite 3* using the geochronology reduction scheme (Paton et al.,  
201 2010) to account for both mass-bias ( $^{207}\text{Pb}/^{206}\text{Pb}$ ) and instrumental drift ( $^{207}\text{Pb}/^{206}\text{Pb}$  and  
202  $^{206}\text{Pb}/^{238}\text{U}$ ). The Tera-Wasserburg data, output from *Iolite*, was then plotted and  $^{206}\text{Pb}/^{238}\text{U}$   
203 ratios of all RMs and unknowns were adjusted such that the primary calcite reference  
204 material—WC-1—yielded an age of 254 Ma (Roberts et al., 2017). This resulted in accurate  
205 dates for both our secondary calcite RM: Duff Brown Tank at  $66.8 \pm 3.4$  Ma (previously  
206 reported 64 Ma; Hill et al., 2016) and a  $^{207}\text{Pb}/^{206}\text{Pb}$  date of zircon RM at  $566.0 \pm 2.8$  Ma  
207 (previously reported 564 Ma; Gehrels et al., 2008). Uncertainty propagation of individual ratios  
208 was assessed by reproducibility of the NIST614 and SL RMs (n=44 in both cases) and added

209 in quadrature such that the MSWD of each weighted average is  $\leq 1$  and that the uncertainty is  
210 no better than 2% (long-term reproducibility); this resulted in propagated uncertainties of 2.5%  
211 and 2% for the  $^{206}\text{Pb}/^{238}\text{U}$  and  $^{207}\text{Pb}/^{206}\text{Pb}$  ratios, respectively. Given that the typical  
212 uncertainties of the  $^{206}\text{Pb}/^{238}\text{U}$  and  $^{207}\text{Pb}/^{206}\text{Pb}$  ratios of the unknowns was  $>10\%$  and  $>3\%$ ,  
213 respectively, the uncertainty propagation on individual ratios had little effect on the calculation  
214 of the final date of ASH-15. The thin section of ASH-15 was measured both parallel to the  
215 length of section (303 spots, and perpendicular to it (101 spots). Data are plotted using Isoplot  
216 (Ludwig, 1998).

### 217 **3.3. LA-ICPMS spot analyses**

218 Analyses were conducted at the Geochronology and Tracers Facility, British Geological  
219 Survey (Nottingham, UK). The instrumentation comprised a New Wave Research 193UC  
220 excimer laser ablation system fitted with a TV2 cell, coupled to a Nu Instruments Attom single  
221 collector inductively coupled plasma mass spectrometer (ICP-MS). The method follows the  
222 protocols described in Roberts and Walker (2016) and Roberts et al. (2017). Laser parameters  
223 varied slightly per session, but typically involve a pre-ablation cleaning spot of 150  $\mu\text{m}$ , fired  
224 at 10 Hz with a fluence of  $\sim 6 \text{ J}/\text{cm}^2$  for 2 seconds, and ablation conditions of 80-100  $\mu\text{m}$  spots,  
225 fired at 10 Hz with a fluence of  $\sim 6-8 \text{ J}/\text{cm}^2$  for 25-30 seconds. A 60 second background is taken  
226 before every set of standard-bracketed analyses, and a 5 second washout is left between each  
227 ablation. Normalization of Pb-Pb ratios is achieved using NIST614 glass (values of Woodhead  
228 and Hergt, 2001), and WC-1 carbonate for Pb-U ratios (Roberts et al., 2017). Data reduction  
229 uses the Time Resolved Analysis function of the Nu Instruments Attolab software, and an excel  
230 spreadsheet, with uncertainty propagation following the recommendations of Horstwood et al.  
231 (2016).

232

### 233 3.4. ID-TIMS U-Pb geochronology

234 Isotope dilution thermal ionization mass spectrometry (ID-TIMS) U-Pb geochronology was  
235 performed at the Institute of Geochemistry and Petrology of ETH Zurich (ETHZ) and at the  
236 Department of Earth Sciences of the University of Geneva (UNIGE). Millimeter-sized chips  
237 of the ASH-15-D and ASH-15-K calcite were extracted using stainless steel tools. Larger chips  
238 were further sub-divided resulting in ~1-7 mg aliquots. Individual chips were transferred into  
239 3 ml Savillex beakers and repeatedly ultrasonically cleaned in ultrapure acetone and water.  
240 Cleaned samples were transferred into pre-cleaned 3 ml Savillex beakers, spiked with ~5-10  
241 mg EARTHTIME ( $^{202}\text{Pb}$ - $^{205}\text{Pb}$ - $^{233}\text{U}$ - $^{235}\text{U}$  tracer solution (Condon et al., 2015) and dissolved  
242 in 6N HCl at 120°C on a hotplate for ~30 minutes to assure complete dissolution and sample-  
243 spike equilibration. Dissolved samples were dried down and redissolved in 1N HBr. Uranium  
244 and Pb were separated using a single-column (50  $\mu\text{l}$ , AG1-X8 resin) HBr-HCl anion exchange  
245 chemistry. The Pb fraction was dried down with a drop of  $\text{H}_3\text{PO}_4$  after a single column pass.  
246 Uranium was dried down, redissolved in 3N HCl and further purified with a HCl-based second  
247 column pass before drying it down with a drop of  $\text{H}_3\text{PO}_4$ . Uranium and Pb were loaded on  
248 outgassed single Re filaments with ~1  $\mu\text{l}$  of Si-gel emitter for thermal ionization mass  
249 spectrometry. Uranium and Pb isotope ratios were measured on a Thermo TRITON Plus at  
250 ETHZ and a Thermo TRITON at UNIGE. Lead isotopes were measured on the axial secondary  
251 electron multiplier employing dynamic peak-hopping routine collecting masses (202), 204, 205,  
252 206, 207 and 208. Measured Pb isotope ratios were corrected for mass fractionation either using  
253 the double spike (ETHZ) or using a mass fractionation factor of  $0.15 \pm 0.03 \text{ \%/amu}$  for single  
254 Pb spiked samples (UNIGE). Uranium isotope ratios were measured as uranium-oxide ( $\text{UO}_2$ )  
255 employing a static measurement routine with Faraday cups connected to amplifiers with  $10^{13}$   
256 ohm feedback resistors (von Quadt et al., 2016; Wotzlaw et al., 2017). Isotope ratios were  
257 corrected for isobaric interferences from minor  $\text{UO}_2$  isotopologues (Wotzlaw et al., 2017) and

258 for mass fractionation using the double spike assuming a  $^{238}\text{U}/^{235}\text{U}$  ratio of  $137.818 \pm 0.045$   
259 (Hiess et al., 2012) for sample and blank. Total procedural Pb blanks for the HBr-based  
260 chemistry at ETHZ are consistently between 0.2 and 0.4 pg. We therefore attribute up to 0.4  
261 pg to laboratory blank with the remaining common Pb being attributed to initial common Pb.  
262 Total procedural blanks measured at UNIGE yielded an average of 1.15 pg that was taken as  
263 the laboratory blank contribution. Data reduction and uncertainty propagation was performed  
264 using Tripoli and an Microsoft Excel-based spreadsheet that uses the algorithms of Schmitz  
265 and Schoene (2007). Isochron calculations were performed using IsoplotR (Vermeesch, 2018).  
266 All uncertainties are reported at 95% confidence ignoring systematic uncertainties associated  
267 with the tracer calibration and decay constants unless otherwise stated.

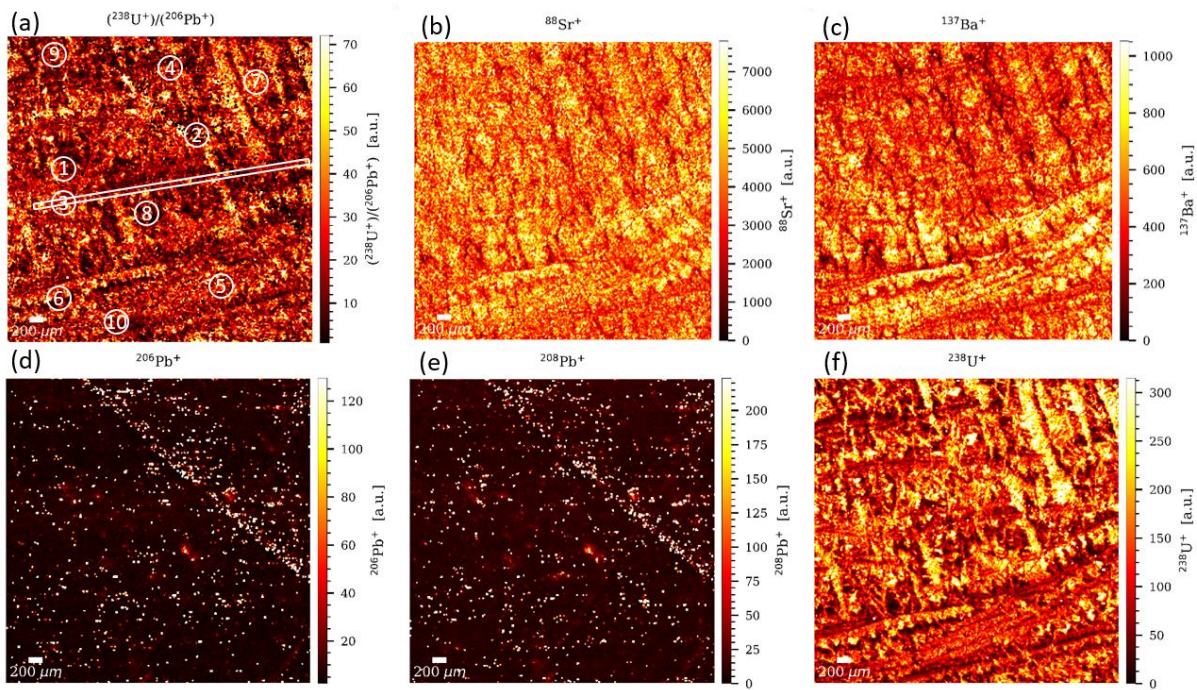
## 268 **4. Results**

269 All analyses were performed on ASH-15-D-K yellow Pliocene layer, abbreviated here as  
270 “ASH-15” unless specification of ASH-15-D, E etc. is indicated. The ASH-15-A-C brown  
271 Pleistocene layer is not part of the ASH-15 suggested reference material.

### 272 **4.1. LA elemental mapping**

273 Elemental mapping for  $^{88}\text{Sr}$ ,  $^{137}\text{Ba}$ ,  $^{206}\text{Pb}$ ,  $^{208}\text{Pb}$ ,  $^{238}\text{U}$  and  $^{238}\text{U}/^{206}\text{Pb}$  ratio shows that the  
274 distribution of most elements is relatively homogeneous (Fig.3), and in good accordance with  
275 the luminescence data. Higher intensities for  $^{238}\text{U}$  and  $^{88}\text{Sr}$  were observed along grain  
276 boundaries and discontinuities, whereas Pb and the rest of the trace elements are more  
277 homogeneously distributed, arguing for steady environmental conditions during the deposition.  
278 Ten random regions of interest (ROI) were selected throughout the sample to mimic 10 spot  
279 analysis carried out at 85-90 microns spot size – just like one would do for U-Pb geochronology.  
280 These ROIs were generated by drawing on the map circular regions with the radius of 85 or 90  
281 microns in diameter. The pixels comprising each ROI were pooled together as representing the

282 equivalent of a single spot analysis. The statistical data for each cluster (data are given in  
 283 supplementary file) were compared. The average values for all pixel data are within 2 standard  
 284 errors and in good agreement, indicating that, at least based on the elemental distribution we  
 285 measured, the sample is relatively homogeneous for a natural sample. To further investigate  
 286 the chemical homogeneity of the sample, a random transect through one of the growth zones  
 287 was drawn and the signal intensities for  $^{238}\text{U}$  were extracted. The transect data also indicate  
 288 that  $^{238}\text{U}$  variations are within 2 standard errors of the average value (full data is available in  
 289 Table S1 in the supplement).



290  
 291 **Figure 3.** Signal intensity maps of ASH-15. for  $^{238}\text{U}/^{206}\text{Pb}$ ,  $^{88}\text{Sr}$ ,  $^{137}\text{Ba}$ ,  $^{206}\text{Pb}$ ,  $^{208}\text{Pb}$ , and  $^{238}\text{U}$   
 292 (a-d). The plotted signal was corrected for blank and analytical drift of the instrumentation.  
 293 Note that each distribution map has its own signal intensity scale. The position of the regions  
 294 of interest and transect is shown in (a). The circles designating the location of the regions of  
 295 interest are not at scale (data is available in Table S1 in the supplement).

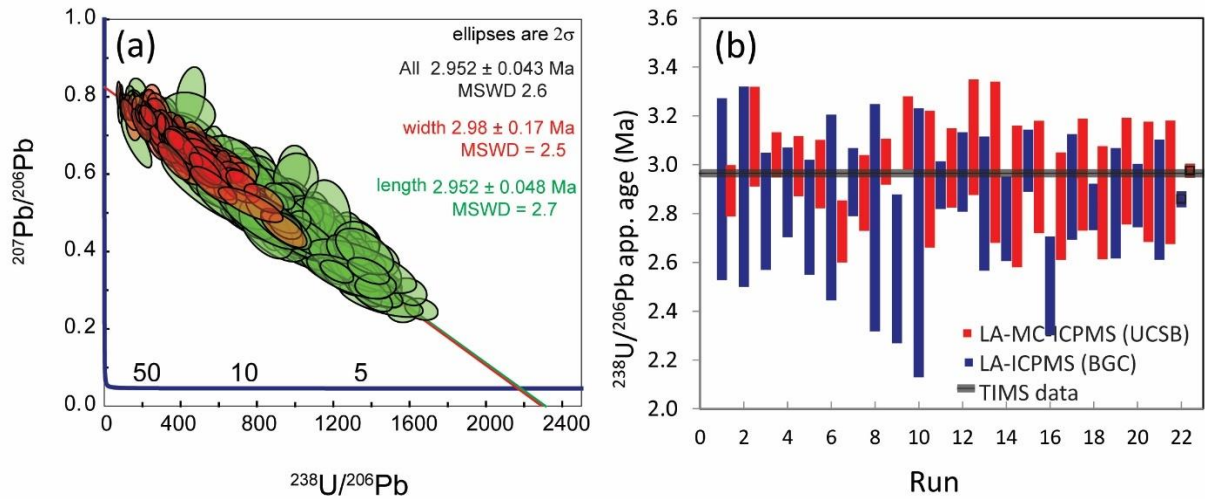
296

## 297 4.2. LA-MC-ICPMS spot analyses

298 Data and calculated ages for the LA-ICPMS transects are shown in Tera-Wasserburg space in  
299 Fig. 4 (n = 379 of 412 total spots). Analyses rejected from the age calculation include those  
300 with  $^{207}\text{Pb}/^{206}\text{Pb}$  uncertainties larger than 0.1% (n = 2) and those with high common-Pb contents  
301 ( $^{208}\text{Pb}$  cps >5000; n = 17). A further 14 spots plotted below the array; these data represent the  
302 first 1–2 mm of spots of the lengthwise transect (lower right in Fig. 2a), and suggest that a  
303 small percent of ASH-15 may behave differently during ablation and/or may have been  
304 subsequently modified after crystallization; upon inspection, this portion of the section contains  
305 more pore space and impurities than the majority of the section. The remaining 379 define a  
306 normally distributed array with a lower intercept age of  $2.952 \pm 0.043$  Ma (MSWD = 2.5),  
307 which is well within uncertainty of the new ID-TIMS data presented (full data is available in  
308 Table S2 in the supplement). The calculated upper intercept of each transect is equivalent and  
309 within 1% of the common Pb composition calculated from the ID-TIMS data. Not surprisingly,  
310 the lengthwise transect reveals a larger spread in common/radiogenic Pb ratios; this transect  
311 crosses more growth zones and has a higher probability of sampling a variety of concentrations  
312 of both Pb and U. Conversely, the more limited spread in common/radiogenic Pb ratios appears  
313 to reflect the limited sampling of growth zones, and would suggest that individual growth zones  
314 contain a relatively limited range of concentrations in U and Pb. The slightly higher MSWD  
315 for the lengthwise transect (2.7) relative to the growth zone transect (2.5) could also reflect  
316 these inherited compositional differences during growth history, and a resulted “mixing” or  
317 “averaging” of different growth phase along calcite continuous growth.

318 Variations of ASH-15 ages during 20 different runs (with 5-30 spot analysis in each) using  
319 both single (ICPMS) and multi-collector (MC-ICPM) are shown in Fig. 4b (full data is available  
320 in Tables S3-S5 in the supplement). The ages are calculated using IsoplotR, not anchored to  
321 specific common-lead, and are not corrected for disequilibrium. Although there is a large

322 scatter in the ages of the different runs the average ages (marked with black box) plot close to  
 323 the new ID-TIMS ages, or are slightly younger in age.



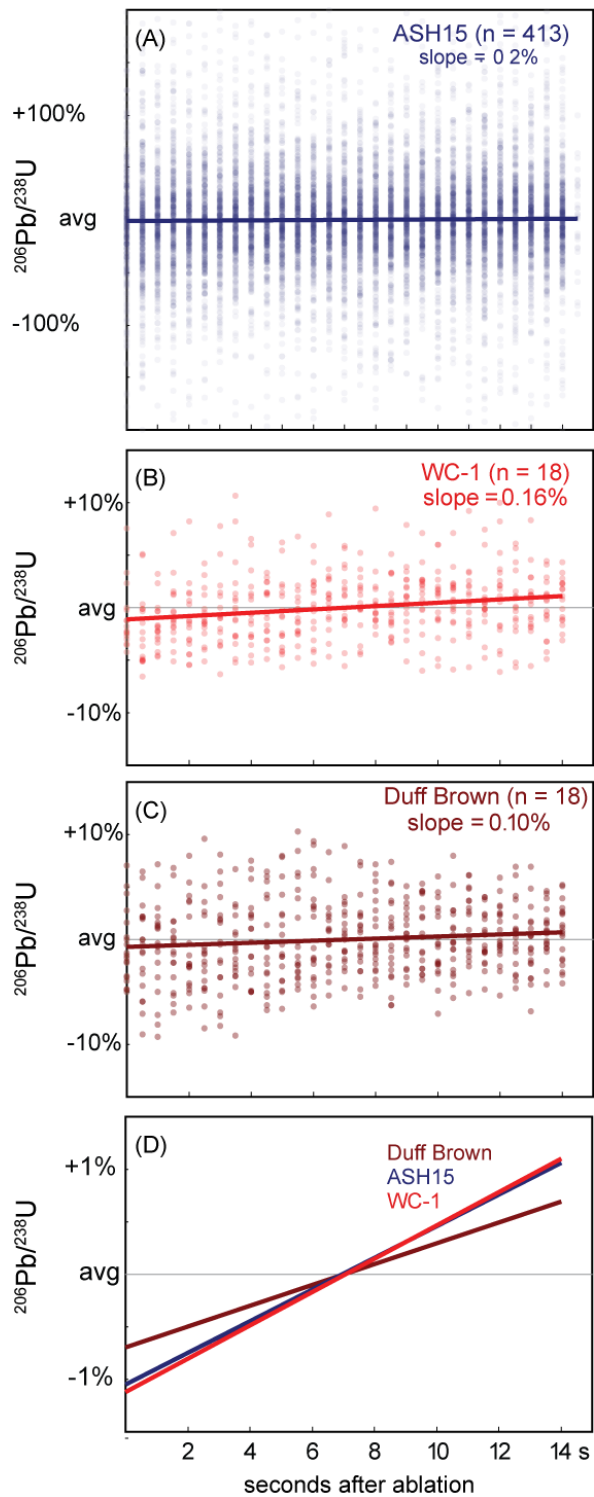
324  
 325 **Figure 4.** LA-MC-ICPMS analyses of calcite ASH-15. (a) Tera-Wasserburg concordia space  
 326 plot (n=385) for spots analysis within lengthwise transect (green) and along growth zone  
 327 transect (red). Calculated age, 2 $\sigma$  error and MSWD are given for both and for all spots together;  
 328 (full data is available in Table S2 in the supplement); (b) Variations of ASH-15 ages during  
 329 different runs using both single and multi-collector ICPMS. Ages are calculated using WC1 as  
 330 primary MS; the new ID-TIMS age is indicated with a grey line; (full data is available in Table  
 331 S3-S5 in the supplement).

### 332 4.3. Down-hole fractionation

333 Reference material is important for correction of both laser-induced elemental fractionation  
 334 (LIEF) and plasma-related ionization efficiency. Ideally, the reference material should  
 335 resemble the unknown samples as much as possible in terms of its chemistry (e.g. Mg and Fe  
 336 content), texture (i.e. micritic, crystalline), and age. The WC1 and ASH15 are both low-Mg  
 337 calcite but they are very different in textures and age. The ASH15 is a ~3 Ma, well-crystallized  
 338 elongated calcite (up to 1 cm) and WC1 is a 254 Ma recrystallized botryoidal calcite, formed

339 after aragonite. Despite these differences, both WC1 and ASH15 display a very similar down-  
340 hole fractionation pattern (Fig. 5d). Fig. 5 shows stacked integration plots of the down-hole  
341 raw  $^{206}\text{Pb}/^{238}\text{U}$  ratio of different RMs including, the ASH15, WC-1, and Duff Brown Tank  
342 (Black and Gulson, 1978). The ASH15 displays much larger scatter in the raw data (Fig. 5a) in  
343 comparison to both WC1 and Duff Brown Tank (Fig. 5b-c), however, the average value yielded  
344 identical down-hole fractionation to that of WC-1 (Fig. 5d). Duff Brown Tank is also consistent  
345 with the down-hole patterns but less steep in comparison to WC1 and ASH15 (Fig. 5d). This  
346 comparison suggests that down-hole fractionation and laser-induced elemental fractionation  
347 (LIEF) are similar among the different RMs. It is thus suggested that differences in measured  
348 and expected  $^{206}\text{Pb}/^{238}\text{U}$  ratios in calcite material are likely to be caused mostly by plasma-  
349 ionization differences between unknown samples and RMs.





350

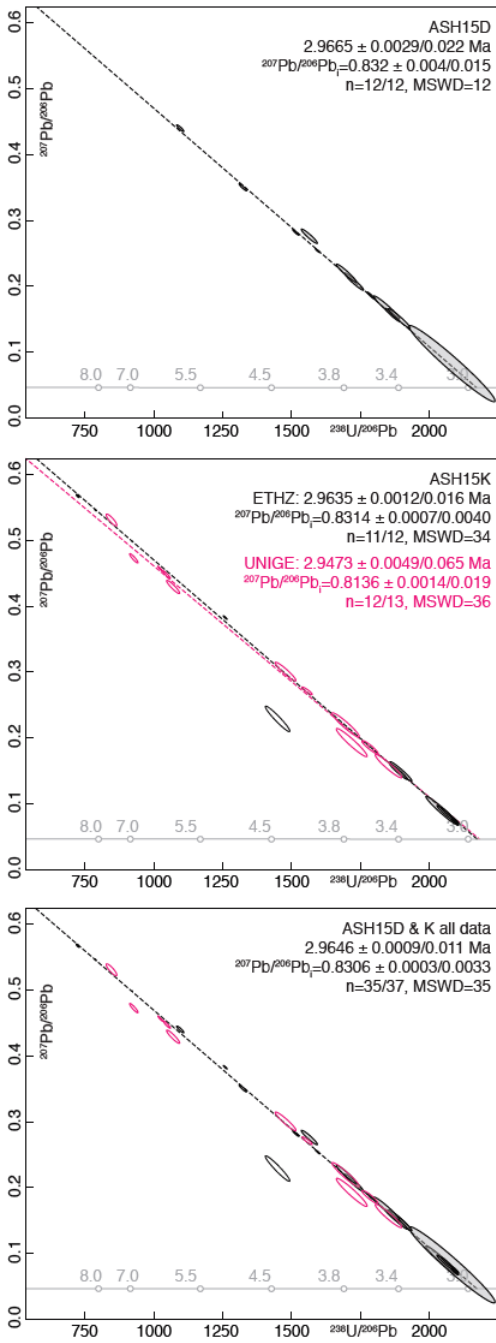
351 **Figure 5.** Stacked integration plots of raw  $^{207}\text{Pb}$ -corrected  $^{206}\text{Pb}/^{238}\text{U}$  ratios for calcite reference  
 352 materials ASH-15, WC-1, and Duff Brown Tank. The low Pb concentration in ASH-15 yields  
 353 more scatter, but average slopes of all RMs are similar, with 1-2% change in age over 10  
 354 seconds (100 pulses) of ablation. The results suggest minimal differences in down-hole  
 355 fractionation of the different RMs.

#### 356 4.4. ID-TIMS results

357 Twelve aliquots of ASH-15D analyzed at ETHZ yielded  $^{238}\text{U}/^{206}\text{Pb}$  ratios between 1096 and  
358 2084 and  $^{207}\text{Pb}/^{206}\text{Pb}$  ratios between 0.0825 and 0.4403 (full data is available in Table S6 in the  
359 supplement). Plotted in Tera-Wasserburg space, these data yield a single isochron with an  
360 initial  $^{207}\text{Pb}/^{206}\text{Pb}$  of  $0.832 \pm 0.015$  (uncertainties are 95% confidence intervals) and a concordia  
361 intercept age of  $2.967 \pm 0.022$  Ma (Fig. 6a). The elevated mean square weighted deviation  
362 (MSWD) of 12 is attributed to minor heterogeneities, most likely in the initial  $^{207}\text{Pb}/^{206}\text{Pb}$  ratio  
363 of the speleothem calcite. Twelve aliquots of ASH-15K analysed at ETHZ returned  $^{238}\text{U}/^{206}\text{Pb}$   
364 ratios between 723 and 2094 and  $^{207}\text{Pb}/^{206}\text{Pb}$  ratios between 0.0720 and 0.5677. In Tera-  
365 Wasserburg space, eleven out of twelve aliquots define a isochron with an initial  $^{207}\text{Pb}/^{206}\text{Pb}$  of  
366  $0.8314 \pm 0.0040$  and a concordia intercept age of  $2.964 \pm 0.016$  Ma (Fig. 6b). A single aliquot  
367 (#5.4) plots significantly below the isochron defined by the other aliquots. The elevated MSWD  
368 of 34 together with the single outlier suggest some heterogeneities in the initial  $^{207}\text{Pb}/^{206}\text{Pb}$  of  
369 the ASH-15K calcite. Thirteen aliquots of ASH-15K analysed at UNIGE (pink color, Fig. 6b)  
370 yielded  $^{238}\text{U}/^{206}\text{Pb}$  ratios between 433 and 1853 and  $^{207}\text{Pb}/^{206}\text{Pb}$  ratios ranging from 0.1856  
371 to 0.6660. Twelve of the thirteen analyses yield best-fit line with an initial  $^{207}\text{Pb}/^{206}\text{Pb}$  of  $0.814$   
372  $\pm 0.019$  and a Concordia intercept age of  $2.947 \pm 0.065$  Ma. The elevated MSWD of 36  
373 confirms the minor heterogeneity of the initial  $^{207}\text{Pb}/^{206}\text{Pb}$ .

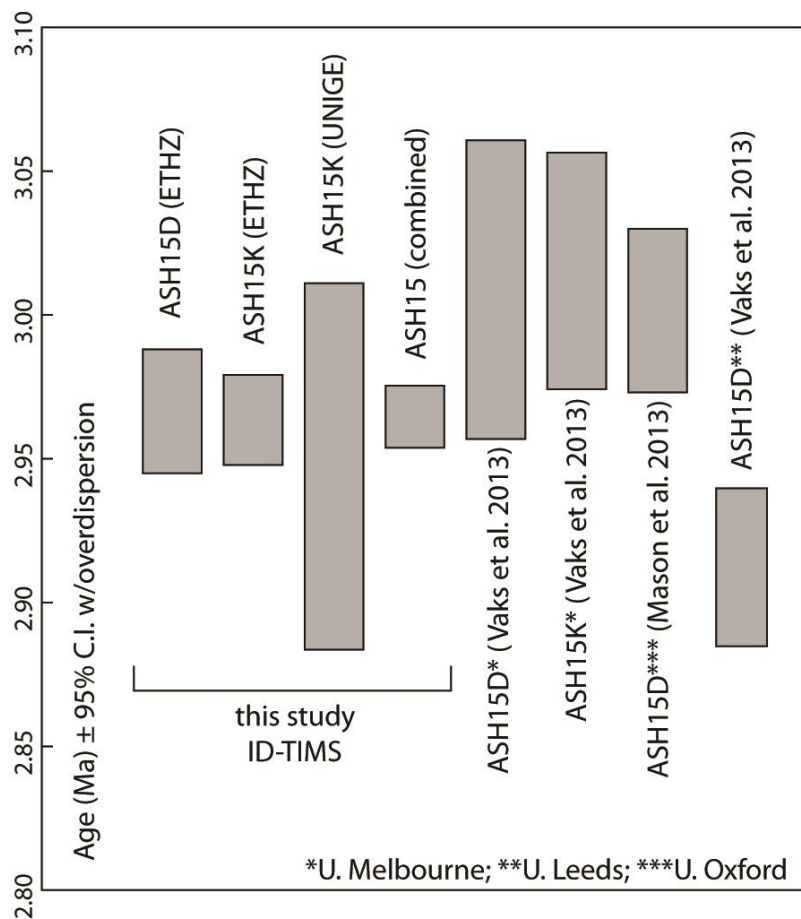
374 The excellent agreement between the ASH-15D and ASH-15K datasets indicates that the entire  
375 speleothem growth layer between these two growth zones is of equivalent age with minor  
376 heterogeneities in the initial  $^{207}\text{Pb}/^{206}\text{Pb}$  ratio and justifies combining the data into a single  
377 isochron regression. The combined isochron, using 35 of 37 analysed aliquots, yields an initial  
378  $^{207}\text{Pb}/^{206}\text{Pb}$  of  $0.8306 \pm 0.0033$  and a concordia intercept age of  $2.965 \pm 0.011$  Ma with a  
379 MSWD of 35 (Fig. 6c). We consider the results of the combined regression as the best reference  
380 value for using ASH-15 as a primary reference material.

381 The new TIMS data provide the most extended bulk investigation of the ASH-15 sample, with  
382 a total of 37 sub-samples that are separated from bottom (K, n=25) to top (D, n=12). The high  
383 MSWD of 35 is suggested to reflect true heterogeneities of the dated material, possibly related  
384 to impurities that are concentrated within grain boundaries (as suggested by CL and elemental  
385 mapping). We re-calculated previously determined isochron ages of Vaks et al. (2013) and  
386 Mason et al. (2013; Fig. 7). We obtained concordia intercept ages of  $3.0088 \pm 0.053$  Ma for  
387 ASH-15-D (MSWD=11; n=5) and  $3.0153 \pm 0.042$  Ma for ASH-15-K (MSWD=14; n=5) of  
388 Vaks et al. (2013) and  $3.0015 \pm 0.029$  for ASH-15-D (MSWD=2; n=5) of Mason et al. (2013).  
389 These ages are largely overlapping within uncertainty with our new ID-TIMS age of  $2.965 \pm$   
390  $0.011$  Ma (Fig. 7; and data in Table S7 in the supplements). The apparent minor systematic  
391 offset towards slightly older ages is attributed to the lower number of aliquots in the MC-  
392 ICPMS datasets combined with the heterogeneous initial Pb isotope composition. For laser  
393 ablation U-Pb work, we recommend the use of the new ID-TIMS age because of the large  
394 number of sub-samples (n=37), and the small aliquots (1-7 mg) that are more representative of  
395 laser-ablation spot analysis. In addition, the use of the precisely and accurately calibrated  
396 EARTHTIME tracer solutions (Condon et al., 2015) and the online mass fractionation  
397 correction provided by the double Pb and double U tracer are an important advantage of this  
398 method. The excellent interlaboratory reproducibility gives us additional confidences that our  
399 ID-TIMS data provide the most accurate characterization of the U-Pb systematics of the ASH-  
400 15 calcite for use as a primary reference material.



401

402 **Figure 6.** ID-TIMS U-Pb results for ASH-15D, ASH-15K, and for both ASH-15D+K  
 403 displayed in Tera-Wasserburg concordia space. Uncertainties on the initial  $^{207}\text{Pb}/^{206}\text{Pb}$  ratios  
 404 and the intercept ages are given as  $2\sigma$  and as 95% confidence intervals including overdispersion  
 405 (Vermeesch, 2018).



406

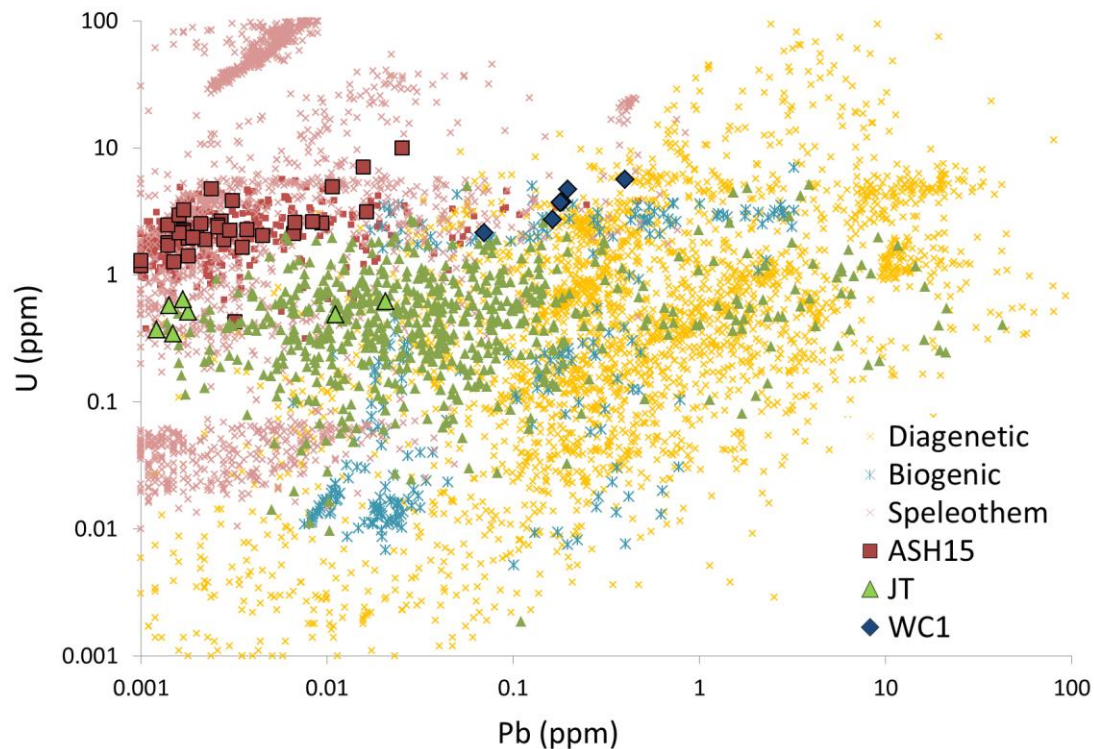
407 **Figure 7.** Previous (re-calculated) and new ages of ASH-15 from isotope-dilution U-Pb  
 408 analysis. All ages are calculated using IsoplotR (Vermeesch, 2018), are not corrected for  
 409 disequilibrium and are not anchored to common-lead specific value (see data in Table S7 in  
 410 the supplements).

#### 411 **4.5. Calcite reference material**

412 The U and Pb concentrations of carbonate materials vary greatly. Data compilation by Roberts  
 413 et al. (2020; this issue) combined hundreds of carbonate samples from different origin such as  
 414 diagenetic, biogenic, speleothem, and vein-fill. This compilation indicates several orders of  
 415 magnitude differences in U and Pb concentrations of the different types of carbonate and the  
 416 heterogeneity of spot analysis within each type or even a single sample. A modified  
 417 representation of their data, excluding calcite vein-fill, which vary throughout the entire

418 compositional range, is shown together with the currently available calcite reference materials  
419 (Fig. 8; and full data in Table S8 in the supplement). Note that both ASH15 and JT, display  
420 much larger heterogeneity when measured by LA-ICPMS (small symbols) relative to ID-TIMS  
421 (large symbols). Despite the high compositional heterogeneity of each of the reference material,  
422 they show minimal overlap and together they cover most of the compositional range of the  
423 presented carbonate material. WC1 (Roberts et al., 2017) with relatively high U and Pb  
424 concentrations can easily be measured on single collector ICPMS (including quadrupole  
425 instruments) and is most appropriate to be used for dating vein-fill and diagenetic carbonates.  
426 In contrast, the ASH15 flowstone, with relatively low Pb and high U concentration that are  
427 better measured on sector-field (MC)-ICPMS is most appropriate for dating speleothem type  
428 carbonates. Finally the JT (Guillong et al., 2020), with moderate U and Pb concentration can  
429 be used on both single- and multi-collector sector field ICPMS instruments and for all types of  
430 carbonate samples. Reference material with high Pb and low U or both low U and Pb  
431 concentrations will further help to cover the full compositional range of carbonate material but  
432 may introduce analytical challenges.

433



434

435 **Figure 8.** U and Pb concentrations of different carbonate samples and available reference  
 436 materials. Large and small symbols for the reference materials indicate ID-TIMS and LA-  
 437 ICPMS analyses, respectively. Note the minimal compositional overlap of the three reference  
 438 materials (ASH15, WC1, and JT). Data for diagenetic, biogenic, and speleothem carbonates  
 439 are from Roberts et al. (2020, this issue). Data for JT standard are from Guillong et al. (2020).

440

## 441 5. Conclusions

442 The ASH-15 speleothem calcite is characterized as a matrix matched reference material for  
 443 LA-ICPMS U-Pb geochronology of calcite. ID-TIMS analyses of small 1-7 mg aliquots of two  
 444 growth zones suggest sufficient homogeneity with a combined intercept age of  $2.965 \pm 0.011$   
 445 Ma and an initial  $^{207}\text{Pb}/^{206}\text{Pb}$  of  $0.8315 \pm 0.0026$ . These data are recommended as the reference  
 446 values for the ASH-15 calcite reference material. The excellent agreement between the two  
 447 growth zones suggest that the entire interval between the two dated layers can be used with the  
 448 same reference age. Compared to other calcite reference material (e.g. WC1), ASH-15 is more

449 homogeneous but has lower radiogenic Pb content and therefore requires more sensitive  
450 instruments (i.e. sector field rather than quadrupole mass spectrometers) to be used as a  
451 reference material.

452

#### 453 **Author's contribution**

454 PN: data processing and writing, JFW: ID-TIMS analysis and writing, MO: ID-TIMS  
455 analysis, AV: sample collection and writing, CS: LA mapping analysis and writing, MS: LA  
456 mapping analysis. NR: LA-ICPMS, data analysis and writing. AKC: LA-MC-ICPMS, data  
457 analysis and writing.

458

#### 459 **Competing interests**

460 The authors declare that they have no conflict of interest.

461

#### 462 **Acknowledgements**

463 We thank reviewers Fernando Corfu and Jon Woodhead as well as editor Axel Gerdes for  
464 constructive comments and suggestions. We thank Bar Elisha for thin-section preparation and  
465 Andrew Mason for constructive discussion. This study was funded by the Israel Science  
466 Foundation, Grant ISF-727/16.



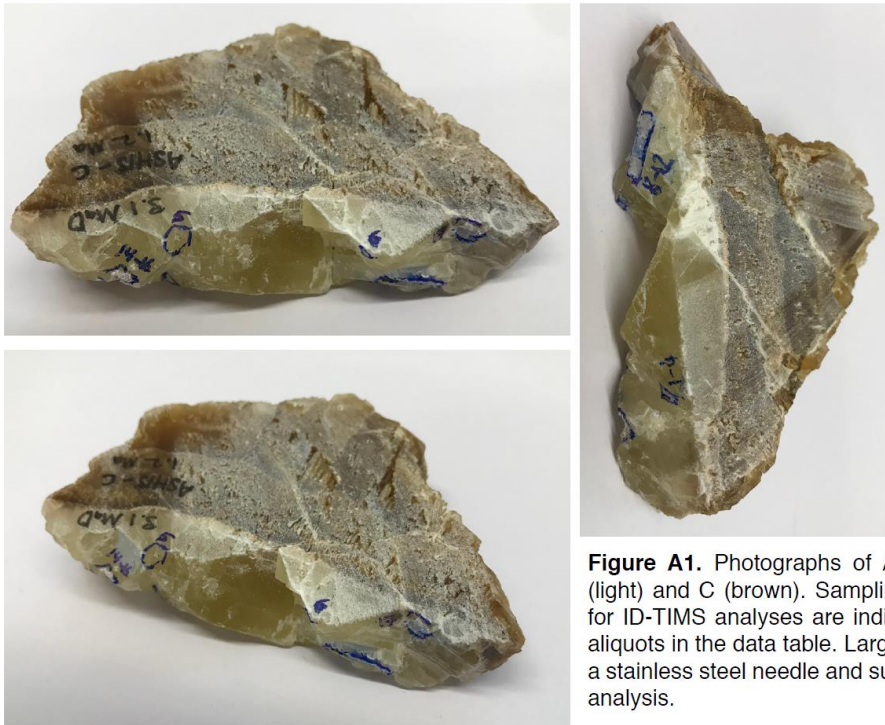


**Figure A1.** Photographs of ASH15 flowstone with layers D (light) and C (brown). Sampling localities of aliquots sampled for ID-TIMS analyses are indicated by numbers matching the aliquots in the data table. Larger pieces were chipped off using a stainless steel needle and subdivided into smaller aliquots for analysis.

468



**Figure A2.** Photographs of ASH15 flowstone with layers K (bottom) to D (top). Sampling localities of aliquots samples for ID-TIMS analyses within layer K are indicated with numbers (n=12) and are matching the aliquots in the data table.

469

470 **References:**

- 471 Anjiang, S., Anping, H., Cheng, T., Liang, F., Wenqing, P., Yuexing, F., and Zhao, J.: Laser ablation  
472 in situ U-Pb dating and its application to diagenesis-porosity evolution of carbonate reservoirs, 46,  
473 1127-1140, 2019.
- 474 Condon, D., Schoene, B., McLean, N., Bowring, S., and Parrish, R.: Metrology and traceability of U–  
475 Pb isotope dilution geochronology (EARTHTIME Tracer Calibration Part I), *Geochimica et*  
476 *Cosmochimica Acta*, 164, 464-480, 2015.
- 477 Coogan, L. A., Parrish, R. R., and Roberts, N. M.: Early hydrothermal carbon uptake by the upper  
478 oceanic crust: Insight from in situ U-Pb dating, *Geology*, 44, 147-150, 2016.
- 479 Crouvi, O., Amit, R., Enzel, Y., and Gillespie, A. R.: Active sand seas and the formation of desert loess,  
480 *Quaternary Science Reviews*, 29, 2087-2098, 2010.
- 481 Godeau, N., Deschamps, P., Guihou, A., Leonide, P., Tendil, A., Gerdes, A., Hamelin, B., and Girard,  
482 J.-P. J. G.: U-Pb dating of calcite cement and diagenetic history in microporous carbonate reservoirs:  
483 Case of the Urgonian Limestone, France, 46, 247-250, 2018.
- 484 Goodfellow, B. W., Viola, G., Bingen, B., Nuriel, P., and Kylander-Clark, A. R. C.: Palaeocene faulting  
485 in SE Sweden from U–Pb dating of slickenfibres calcite, *Terra Nova*, n/a-n/a, 10.1111/ter.12280, 2017.
- 486 Guillong, M., Wotzlaw, J. F., Looser, N., and Laurent, O.: New analytical and data evaluation protocols  
487 to improve the reliability of U-Pb LA-ICP-MS carbonate dating, *Geochronology Discuss.*, 2020, 1-17,  
488 10.5194/gchron-2019-20, 2020.
- 489 Hansman, R. J., Albert, R., Gerdes, A., and Ring, U.: Absolute ages of multiple generations of brittle  
490 structures by U-Pb dating of calcite, *Geology*, 46, 207-210, 2018.
- 491 Hiess, J., Condon, D. J., McLean, N., and Noble, S. R.:  $^{238}\text{U}/^{235}\text{U}$  systematics in terrestrial uranium-  
492 bearing minerals, *Science*, 335, 1610-1614, 2012.
- 493 Holdsworth, R., McCaffrey, K., Dempsey, E., Roberts, N., Hardman, K., Morton, A., Feely, M., Hunt,  
494 J., Conway, A., and Robertson, A.: Natural fracture propping and earthquake-induced oil migration in  
495 fractured basement reservoirs, *Geology*, 47, 700-704, 2019.
- 496 Horstwood, M. S., Košler, J., Gehrels, G., Jackson, S. E., McLean, N. M., Paton, C., Pearson, N. J.,  
497 Sircombe, K., Sylvester, P., and Vermeesch, P.: Community-derived standards for LA-ICP-MS U-(Th-)  
498 Pb geochronology—Uncertainty propagation, age interpretation and data reporting, *Geostandards and*  
499 *Geoanalytical Research*, 40, 311-332, 2016.
- 500 Li, Q., Parrish, R., Horstwood, M., and McArthur, J.: U–Pb dating of cements in Mesozoic ammonites,  
501 *Chemical Geology*, 376, 76-83, 2014.
- 502 MacDonald, J., Faithfull, J., Roberts, N., Davies, A., Holdsworth, C., Newton, M., Williamson, S.,  
503 Boyce, A., John, C. J. C. t. M., and Petrology: Clumped-isotope palaeothermometry and LA-ICP-MS  
504 U–Pb dating of lava-pile hydrothermal calcite veins, 174, 63, 2019.
- 505 Mason, A. J., Henderson, G. M., and Vaks, A.: An Acetic Acid-Based Extraction Protocol for the  
506 Recovery of U, Th and Pb from Calcium Carbonates for U-(Th)-Pb Geochronology, *Geostandards and*  
507 *Geoanalytical Research*, 37, 261-275, 10.1111/j.1751-908X.2013.00219.x, 2013.

508 Nuriel, P., Weinberger, R., Kylander-Clark, A. R. C., Hacker, B. R., and Craddock, J. P.: The onset of  
509 the Dead Sea transform based on calcite age-strain analyses, *Geology*, 45, 587-590, 10.1130/g38903.1,  
510 2017.

511 Nuriel, P., Craddock, J., Kylander-Clark, A. R., Uysal, I. T., Karabacak, V., Dirik, R. K., Hacker, B. R.,  
512 and Weinberger, R. J. G.: Reactivation history of the North Anatolian fault zone based on calcite age-  
513 strain analyses, 47, 465-469, 2019.

514 Parrish, R. R., Parrish, C. M., and Lasalle, S.: Vein calcite dating reveals Pyrenean orogen as cause of  
515 Paleogene deformation in southern England, *Journal of the Geological Society*, 10.1144/jgs2017-107,  
516 2018.

517 Piccione, G., Rasbury, E. T., Elliott, B. A., Kyle, J. R., Jaret, S. J., Acerbo, A. S., Lanzirotti, A.,  
518 Northrup, P., Wooton, K., and Parrish, R. R.: Vein fluorite U-Pb dating demonstrates post-6.2 Ma rare-  
519 earth element mobilization associated with Rio Grande rifting, *Geosphere*, 15, 1958-1972, 2019.

520 Ring, U., and Gerdes, A.: Kinematics of the Alpenrhein-Bodensee graben system in the Central Alps:  
521 Oligocene/Miocene transtension due to formation of the Western Alps arc, *Tectonics*, 35, 1367-1391,  
522 10.1002/2015TC004085/abstract, 2016.

523 Roberts, N. M., and Walker, R. J.: U-Pb geochronology of calcite-mineralized faults: Absolute timing  
524 of rift-related fault events on the northeast Atlantic margin, *Geology*, 44, 531-534, 2016.

525 Roberts, N. M., Rasbury, E. T., Parrish, R. R., Smith, C. J., Horstwood, M. S., and Condon, D. J.: A  
526 calcite reference material for LA-ICP-MS U-Pb geochronology, *Geochemistry, Geophysics, Geosystems*,  
527 2017.

528 Roberts, N. M. W., Drost, K., Horstwood, M. S. A., Condon, D. J., Chew, D., Drake, H., Milodowski,  
529 A. E., McLean, N. M., Smye, A. J., Walker, R. J., Haslam, R., Hodson, K., Imber, J., Beaudoin, N., and  
530 Lee, J. K.: Laser ablation inductively coupled plasma mass spectrometry (LA-ICP-MS) U-Pb carbonate  
531 geochronology: strategies, progress, and limitations, *Geochronology*, 2, 33-61, 10.5194/gchron-2-33-  
532 2020, 2020.

533 Schmitz, M. D., and Schoene, B.: Derivation of isotope ratios, errors, and error correlations for U-Pb  
534 geochronology using  $^{205}\text{Pb}$ - $^{235}\text{U}$ -( $^{233}\text{U}$ )-spiked isotope dilution thermal ionization mass  
535 spectrometric data, *Geochemistry, Geophysics, Geosystems*, 8, 2007.

536 Vaks, A., Bar-Matthews, M., Matthews, A., Ayalon, A., and Frumkin, A.: Middle-Late Quaternary  
537 paleoclimate of northern margins of the Saharan-Arabian Desert: reconstruction from speleothems of  
538 Negev Desert, Israel, *Quaternary Science Reviews*, 29, 2647-2662, 2010.

539 Vaks, A., Woodhead, J., Bar-Matthews, M., Ayalon, A., Cliff, R. A., Zilberman, T., Matthews, A., and  
540 Frumkin, A.: Pliocene-Pleistocene climate of the northern margin of Saharan-Arabian Desert recorded  
541 in speleothems from the Negev Desert, Israel, *Earth and Planetary Science Letters*, 368, 88-100,  
542 <http://dx.doi.org/10.1016/j.epsl.2013.02.027>, 2013.

543 van Elteren, J. T., Šelih, V. S., Šala, M., Van Malderen, S. J., and Vanhaecke, F.: Imaging artifacts in  
544 continuous scanning 2D LA-ICPMS imaging due to nonsynchronization issues, *Analytical chemistry*,  
545 90, 2896-2901, 2018.

546 van Elteren, J. T., Šelih, V. S., and Šala, M.: Insights into the selection of 2D LA-ICP-MS (multi)  
547 elemental mapping conditions, *Journal of Analytical Atomic Spectrometry*, 34, 1919-1931, 2019.

548 van Malderen, S.: Optimization of methods based on laser ablation-ICP-mass spectrometry (LA-ICP-  
549 MS) for 2-D and 3-D elemental mapping, Ghent University, 2017.

- 550 Vermeesch, P.: IsoplotR: A free and open toolbox for geochronology, *Geoscience Frontiers*, 2018.
- 551 von Quadt, A., Wotzlaw, J.-F., Buret, Y., Large, S. J., Peytcheva, I., and Trinquier, A.: High-precision  
552 zircon U/Pb geochronology by ID-TIMS using new 10 13 ohm resistors, *Journal of Analytical Atomic*  
553 *Spectrometry*, 31, 658-665, 2016.
- 554 Woodhead, J., and Petrus, J. J. G.: Exploring the advantages and limitations of in situ U–Pb carbonate  
555 geochronology using speleothems, 1, 69-84, 2019.
- 556 Woodhead, J. D., and Hergt, J. M.: Strontium, neodymium and lead isotope analyses of NIST glass  
557 certified reference materials: SRM 610, 612, 614, *Geostandards Newsletter*, 25, 261-266, 2001.
- 558 Wotzlaw, J.-F., Buret, Y., Large, S. J., Szymanowski, D., and von Quadt, A.: ID-TIMS U–Pb  
559 geochronology at the 0.1‰ level using 10 13 Ω resistors and simultaneous U and 18 O/16 O isotope  
560 ratio determination for accurate UO 2 interference correction, *Journal of Analytical Atomic*  
561 *Spectrometry*, 32, 579-586, 2017.
- 562